Hybrid interferometric near infrared spectroscopy (hybrid iNIRS) enables time-of-flight–resolved non-invasive blood flow monitoring in humans in vivo

Marcin Marzejon

Institute of Physical Chemistry, Polish Academy of Sciences

Dawid Borycki

dborycki@ichf.edu.pl

Institute of Physical Chemistry, Polish Academy of Sciences

Article

Keywords:

Posted Date: January 8th, 2026

DOI: https://doi.org/10.21203/rs.3.rs-8492157/v1

Additional Declarations: No competing interests reported.

Hybrid interferometric near infrared spectroscopy (hybrid iNIRS) enables time-of-flight–resolved non-invasive blood flow monitoring in humans *in vivo*

Marcin Marzejon[1] and Dawid Borycki[1,2,*]

[1] *Institute of Physical Chemistry, Polish Academy of Sciences, Kasprzaka 44/52, 01-224 Warsaw, Poland*
[2] *International Centre for Translational Eye Research, Skierniewicka 10A, 01-230 Warsaw, Poland*
** Corresponding author, dborycki@ichf.edu.pl*

Abstract Interferometric near-infrared spectroscopy (iNIRS) uniquely offers time-of-flight (TOF) resolution for depth-resolved optical property and blood-flow assessment in tissue, but single-mode collection constrains photon throughput and single-channel implementations impose stringent analog bandwidth and digitization rates to resolve both TOF and speckle dynamics. Conversely, continuous-wave parallel interferometric NIRS (CW-πNIRS) boosts photon detection via spatial multiplexing on camera sensors, yet sacrifices TOF information and remains limited by camera readout. Here we reconcile these trade-offs with a hybrid swept-source, hybrid iNIRS platform that combines TOF encoding with multi-speckle, heterodyne detection. Liquid-phantom experiments map the trade-space among sweep speed, and speckle decorrelation, indicating that sweep rates ≥10 kHz are required to outpace decorrelation while preserving TOF contrast. *In vivo* forearm and forehead measurements demonstrate depth-resolved blood flow measurements during cuff occlusion. By simultaneously overcoming photon-starvation and electronic-bandwidth ceilings, this approach establishes a new operating regime for diffuse optical monitoring and provides a scalable hardware foundation for haemodynamic sensing *in vivo*.

Introduction

Monitoring cerebral blood flow (CBF) and oxygenation is fundamental for detecting hypoxia, ischemia, impaired autoregulation, and other threats to brain health in vulnerable patients from preterm newborns to adults with head injury or stroke [1-5]. The ideal tool should operate non-invasively, continuously at the bedside, and with both depth sensitivity and quantitative accuracy [2, 6]. Near-infrared spectroscopy (NIRS) has long been the clinical favourite because tissue is relatively transparent to 650–900 nm light [6-8], enabling centimeter-scale penetration and cortical interrogation without burr-holes or radiation [9].

Conventional continuous-wave NIRS (CW-NIRS) is the most widely used form of NIRS for functional and clinical monitoring [10, 11]. By measuring intensity changes at multiple wavelengths, CW-NIRS estimates relative concentration changes of oxy- and deoxy-haemoglobin and provides robust, real-time readouts of relative oxygenation and total haemoglobin volume. However, three shortcomings limit its utility. First, CW-NIRS infers CBF only indirectly through changes in oxygen saturation, so small or rapid perfusion shifts may be missed [12]. Second, intensity measurements integrate over all photon trajectories, allowing superficial circulation to mask deeper cortical signals [9, 13, 14]. Third, without time-of-flight (TOF) or phase

information, CW-NIRS cannot recover absolute absorption and scattering coefficients (μ_a,μ_s') or absolute flow indices [15-19].

To directly probe microvascular dynamics, diffuse correlation spectroscopy (DCS) analyzes speckle intensity fluctuations induced by red blood cell motion, yielding a blood-flow index (BFI) independent of oxygenation [1, 20, 21]. Interferometric NIRS (iNIRS) extends this approach by detecting the optical field rather than intensity, which allows direct access to the field autocorrelation and simplifies analysis [22-27]. Unlike time-domain DCS (TD-DCS), which recovers field correlations indirectly via the Siegert relation [28-30], iNIRS directly measures the complex temporal coherence function of multiply scattered light [23]. Nevertheless, both DCS and iNIRS usually rely on single-mode fibre detection, which restricts photon throughput and makes them photon-starved at centimeter-scale source–detector separations required for adult cortex [20, 21, 31]. Using multiple fibres can alleviate this but adds cost, complexity, and high data rates [32].

Parallel detection strategies have been proposed to overcome photon limitations by capturing many speckle modes simultaneously. These include single-photon avalanche diode (SPAD) arrays [33], speckle contrast optical spectroscopy (SCOS) [34], and interferometric diffusing-wave spectroscopy (iDWS) [35]. Continuous-wave parallel interferometric NIRS (CW-πNIRS) [36] combines diffuse tissue light with a reference beam on a camera sensor, enabling multi-speckle heterodyne detection [36]. This boosts signal-to-noise ratio (SNR) through spatial averaging but sacrifices TOF discrimination, since camera readout rates are far slower than the digitizers used in swept-source iNIRS [22, 37]. Thus, a trade-off remains: single-channel iNIRS offers depth resolution but is photon-starved, while CW-πNIRS achieves high photon throughput but no TOF sectioning.

A compact theoretical framework clarifies these contrasts. In iNIRS, the detector records the spectral interferogram at optical frequency ν and sweep index t_d:

$$S(\boldsymbol{r}, \nu, t_d) = S_{DC}(\boldsymbol{r}, \nu, t_d) + 2Re[W_{rs}(\boldsymbol{r}, \nu, t_d)], \tag{1}$$

where S_{DC} is the DC background and W_{rs} is the cross-spectral density of reference and sample fields. After resampling to uniform wavenumber and Fourier transforming, one obtains the mutual coherence function,

$$\Gamma_{rs}(\boldsymbol{r}, \tau_s, t_d) = \langle U_r^*(\boldsymbol{r}, t_s, t_d) U_s(\boldsymbol{r}, t_s + \tau_s, t_d) \rangle_{t_s}, \tag{2}$$

with TOF τ_s as the conjugate variable to ν. Autocorrelation across sweeps yields the TOF-resolved field correlation,

$$G_1^{(\mathrm{iNIRS})}(\boldsymbol{r}, \tau_s, \tau_d) = \langle \Gamma_{rs}^*(\boldsymbol{r}, \tau_s, t_d) \Gamma_{rs}(\boldsymbol{r}, \tau_s, t_d + \tau_d) \rangle_{t_d}. \tag{3}$$

where lag τ_d is set by the sweep rate. In parallel iNIRS (πNIRS), this quantity is spatially averaged across pixels to boost SNR. If TOF is integrated out, one recovers the continuous-wave limit,

$$G_1^{(\mathrm{CW-\pi NIRS})}(\tau_d) = \int_0^\infty d\tau_s \, G_1^{(\pi\mathrm{NIRS})}(\tau_s, \tau_d), \tag{4}$$

which corresponds to conventional CW-πNIRS. Namely, high photon throughput but no depth discrimination.

The TOF-resolved field autocorrelation $G_1^{(\mathrm{iNIRS})}(\boldsymbol{r}, \tau_s, \tau_d)$ is the central observable in interferometric NIRS and provides two complementary readouts. First, setting the lag to zero yields the temporal point spread function (TPSF),

$$I_s(\tau_s) \;=\; G_1^{(\mathrm{iNIRS})}(r, \tau_s, \tau_d = 0), \tag{5}$$

which represents the distribution of photon times-of-flight. By fitting the TPSF with a diffusion-theory model convolved with the instrument response, one can recover the bulk optical properties of tissue, namely the absorption coefficient μ_a and the reduced scattering coefficient $\mu_s{}'$.

Second, for finite lags $\tau_d > 0$, the decay of $G_1^{(\mathrm{iNIRS})}(\boldsymbol{r}, \tau_s, \tau_d)$ encodes temporal decorrelation of speckle fields due to moving scatterers such as red blood cells. According to Diffusing Wave Spectroscopy (DWS) theory, the decorrelation rate is proportional to the blood-flow index (BFi). Importantly, quantitative recovery of BFi requires knowledge of $\mu_s{}'$ from the TPSF, since the rate of decorrelation scales with both photon path length (via τ_s) and scattering strength.

Thus, a single interferometric measurement simultaneously yields static optical properties (μ_a,$\mu_s{}'$) through the TPSF and dynamic blood-flow information (BFi) through autocorrelation analysis. This dual role of $G_1^{(\mathrm{iNIRS})}$ underpins the power of iNIRS to unify absorption, scattering, and flow sensing within one framework.

In swept-source iNIRS, the autocorrelation lag step is fixed by the sweep rate ($\delta\tau_d \;=\; 1/f_l$), which exposes two core trade-offs. Bandwidth trade-off: increasing the tuning range $\Delta\lambda$ sharpens TOF resolution (Eq. (S12)) but reduces the maximum usable TOF window, limiting sensitivity to deeper tissue. Speed trade-off: increasing the sweep rate f_l improves temporal sampling of fast dynamics (Eq. (S15)) but narrows the TOF window (Eq. (S14)) unless the detector sampling rate f_s is proportionally increased. Raising f_s requires wider-bandwidth digitizers or faster cameras, adding cost and complexity. In practice, iNIRS must balance fine TOF resolution for optical-property fits, a sufficient TOF window (Eq. (S14)) to reach cortex, and high temporal sampling for flow – all within the limits of laser tuning mechanics and detection electronics. Detailed theoretical limits and design trade-offs are derived in the Supplementary Information.

For cortical sensing, diffusion-theory analyses [16, 17] suggest DTOF windows of 1–5 ns at typical source–detector separations. Because iNIRS operates with a narrower instrument response (15-50 ps FWHM versus 200–500 ps in TD-NIRS), shorter separations can be used, and a design target of $\tau_{s,target} = 1 - 1.5\ ns$ sufficient to reach cortex. The maximum sweep rate is then constrained by the requirement that the sampling-determined TOF window exceed this target. This ceiling scales linearly with sampling rate, quadratically with centre wavelength, and inversely with tuning bandwidth (Eq. (S17)). Thus, widening $\Delta\lambda$ improves TOF resolution but lowers the maximum sweep rate unless f_s is proportionally raised. In our parallel iNIRS prototype, the dominant limit is the camera line rate ($f_s \;=\; 1.1\ \mathrm{MHz}$), which restricts sweep rates to the tens-of-kilohertz regime (see Supplementary Information).

Current implementations each fail at one corner of this trade space. Single-mode iNIRS achieves sub-20 ps TOF resolution but is photon-starved at centimeter-scale separations, forcing >0.5-1 s integration times and blurring fast haemodynamics. A straightforward solution is to add multiple

SMFs, but this increases system cost, alignment complexity, and data rate. Parallel iNIRS (πNIRS) improves throughput by collecting thousands of speckle modes on a camera, but MHz-class frame rates restrict sweep speeds to ~20 kHz – insufficient to capture nanosecond-scale decorrelation dynamics. Continuous-wave πNIRS further boosts photon efficiency but sacrifices TOF sectioning altogether, yielding only depth-averaged flow indices. In short, iNIRS provides depth but too few photons, while πNIRS and CW-πNIRS provide photons but no usable TOF discrimination.

To overcome these complementary bottlenecks, we developed a hybrid interferometric architecture that distributes a single swept source across three coordinated detection paths (Fig. 1). A single-mode iNIRS arm digitized at 125 MS/s provides precise wavenumber calibration, phase stability, and sub-20 ps TOF fidelity. A parallel-camera arm images many speckle modes at 1.1 MHz, boosting photon throughput and SNR without fibre bundles or detector arrays. An auxiliary reference interferometer ensures real-time k-linearization and source stability. Together, these arms enable practical sweep rates of 50–100 kHz while maintaining nanosecond TOF resolution, balancing photon efficiency with temporal sampling. This hybrid design addresses the electronic and optical ceilings of interferometric NIRS and establishes a compact, fibre-sparse platform suitable for bedside cerebral and peripheral blood-flow monitoring.

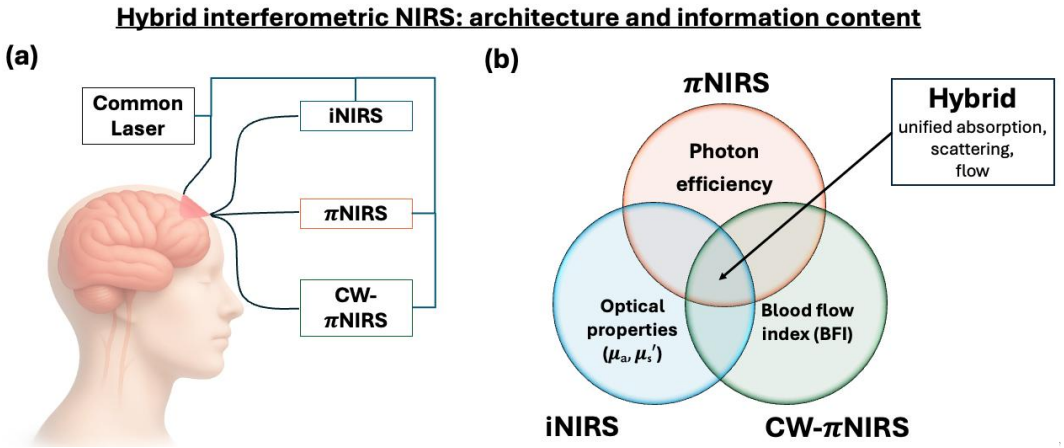

Fig. 1. Hybrid interferometric NIRS: architecture and information content. (a) Conceptual system architecture. A single swept-source laser is distributed into three coordinated detection paths: a single-mode iNIRS arm providing picosecond TOF resolution and optical-property fits (μ_a, μ_s'); a parallel πNIRS arm that captures thousands of speckle modes for photon efficiency; and a CW-πNIRS mode that yields robust blood-flow indices (BFI) from TOF-integrated correlations. (b) Information-space Venn diagram illustrating the strengths and limitations of each modality. iNIRS recovers optical absorption and scattering, CW-πNIRS provides flow indices, and πNIRS improves photon throughput but with limited TOF sectioning and slow sweep rates. The hybrid approach combines all three, enabling unified measurement of absorption, scattering, and flow within a single platform.

Results

Time-of-flight resolution and sensing range

We quantified the TOF performance of the hybrid iNIRS instrument using a 1-m multimode patch cable. For each acquisition, we reconstructed the temporal point spread function (TPSF) and

defined the TOF resolution $\delta\tau_s$ as the full width at half maximum (FWHM) of the TPSF peak. To assess sweep-rate effects, we varied the laser sweep frequency f_l from 1–15 kHz while holding the diode modulation current fixed at $I_{mod} = 3.12$ mA (tuning range $\Delta\lambda = 38$ pm). Increasing f_l broadened the TPSF and increased $\delta\tau_s$, consistent with the expected degradation in TOF resolution at higher sweep rates (Fig. 2A). Across conditions, πNIRS produced systematically broader TPSFs than iNIRS, consistent with its lower per-pixel SNR.

To isolate the role of tuning range, we fixed $f_l = 1$ kHz and increased I_{mod} to expand the laser tuning range $\Delta\lambda$. Larger $\Delta\lambda$ narrowed the TPSF and reduced $\delta\tau_s$ (Fig. 2B), while the πNIRS TPSFs remained broader than iNIRS. Increasing $\Delta\lambda$ also shortened the unambiguous TOF imaging range, and higher f_l further reduced this range (Fig. 2A, right), highlighting the trade-off between depth sectioning (set primarily by $\Delta\lambda$), laser sweep rate (set by f_l), and the usable TOF window. In subsequent *in vivo* measurements, f_l and $\Delta\lambda$ were therefore chosen to balance temporal sampling, TOF resolution, and TOF range for blood-flow monitoring.

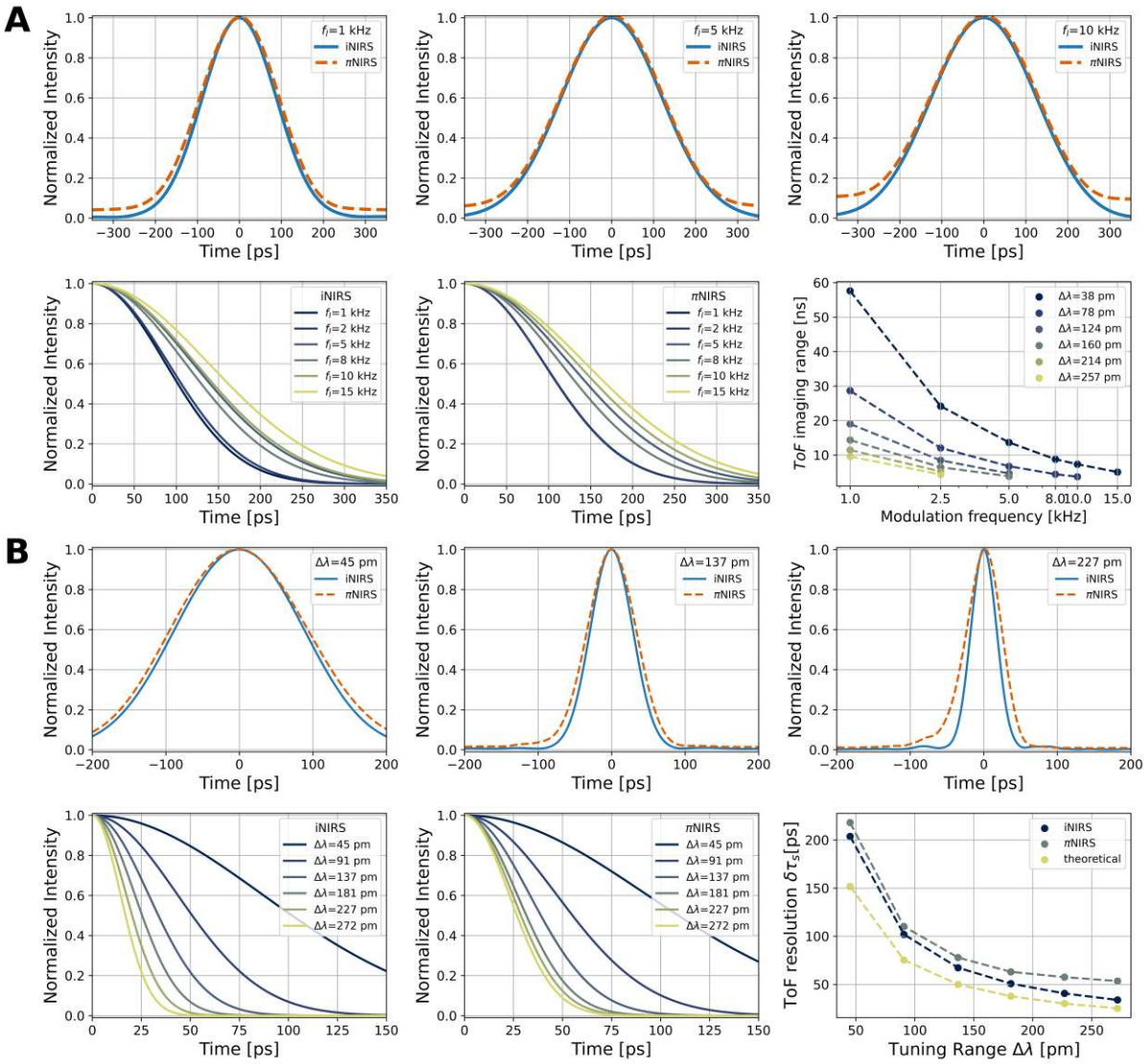

Fig. 2. Sweep frequency and tuning range determine time-of-flight (TOF) resolution and unambiguous TOF window in the hybrid iNIRS system. (**A**) Sweep-frequency dependence. Representative TPSFs at f_l = 1, 5, and 10 kHz (top row) and normalized TPSFs for f_l = 1–15 kHz (bottom row; iNIRS at left, πNIRS at center) show progressive TPSF

broadening with increasing sweep frequency. The corresponding maximum unambiguous TOF window, $\tau_{s,max}$, decreases with increasing l and varies with laser tuning range $\Delta\lambda$ (steered by the modulation current I_{mod}; bottom right). (**B**) Tuning-range dependence. Representative TPSFs for tuning ranges $\Delta\lambda$ = 65, 137, and 227 pm (top row) and normalized TPSFs for multiple $\Delta\lambda$ values (bottom row; iNIRS at left, πNIRS at center) show TPSF narrowing as $\Delta\lambda$ increases. The measured $\delta\tau_s$ versus $\Delta\lambda$ for iNIRS and πNIRS is compared with the theoretical prediction (bottom right). Overall, increasing f_l degrades TOF resolution, whereas increasing $\Delta\lambda$ improves TOF resolution but shortens the usable TOF window.

Phantom decorrelation dynamics

We next investigated the effect of sweep rate on the ability to resolve sample dynamics in tissue-mimicking liquid phantoms. At low sweep rates (e.g., 1–10 kHz), the fringe pattern became chirped, and the TPSF broadened, consistent with the expected Doppler-like distortion [38]. Under these conditions, the first autocorrelation lag already decayed to baseline, preventing reliable recovery of the dynamics.

As the sweep rate increased (20–100 kHz), the TPSF sharpened and the field autocorrelation $g_1(\tau_{s,}\tau_d)$ could be recovered over progressively longer time-of-flights (Fig. 3). At sufficiently high sweep rates, the TOF-resolved iNIRS curves at the centroid converged toward the CW-πNIRS reference, which provides a TOF-integrated but finely sampled decorrelation measurement at 1.1 MHz. This convergence confirms that, when sweep speed is fast enough to outpace sample decorrelation, swept-source iNIRS recovers the same dynamics as CW-πNIRS while also preserving TOF discrimination.

These results highlight the trade-off between resolution and photon statistics. Increasing sweep speed is necessary to capture fast decorrelation, but excessively high rates reduce photon counts per sweep and can bias flow indices upward. Having access to both swept-source and CW-πNIRS modes in the hybrid platform provides a built-in check. If centroid of the TOF-gated decorrelation agrees with the CW-πNIRS reference, the chosen sweep regime is adequate.

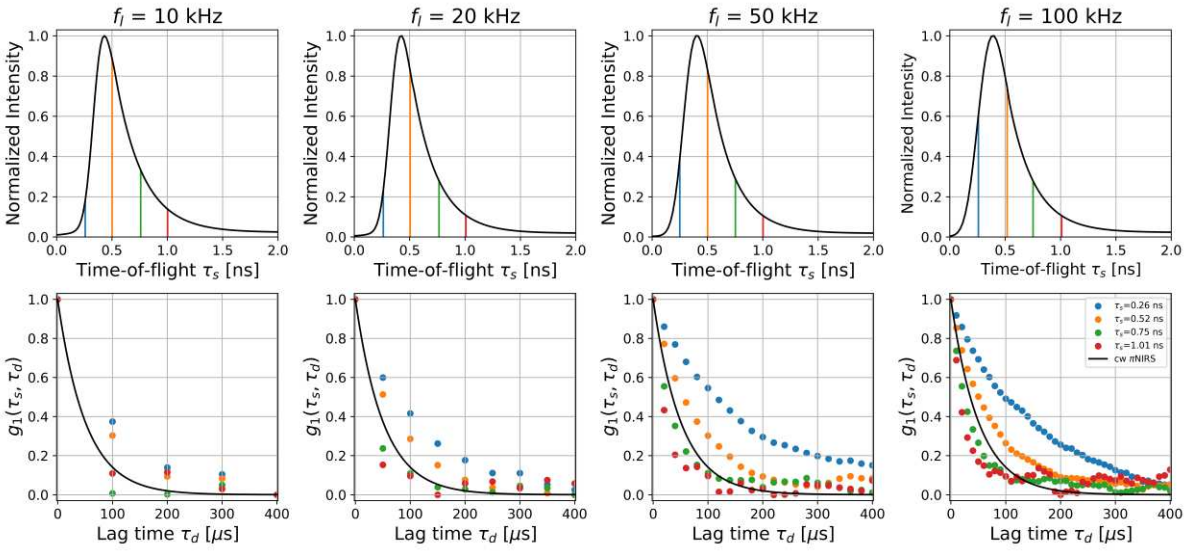

Fig. 3. Phantom decorrelation dynamics across sweep rates. (Top) TPSFs at 10, 20, 50, and 100 kHz showing broadening at slow sweeps and sharpening at higher speeds. (Bottom) Corresponding g_1 curves. CW-πNIRS reference (black) represents TOF-integrated decorrelation at 1.1 MHz. Convergence of swept-source iNIRS curves toward the CW reference indicates adequate sweep rate.

Based on phantom experiments, we selected a sweep rate of 50 kHz for *in vivo* measurements. At lower sweep rates (≤10 kHz), the decorrelation dynamics were undersampled and $g_1(\tau_{s,}\tau_d)$ collapsed at the first lag for the late times-of-flight ($\tau_s > 700$ ps). At higher rates (~100 kHz) the reduced photon counts per sweep caused excess noise that biased the correlation toward faster apparent decay. The intermediate regime of 50 kHz therefore provided the best balance between temporal sampling and signal-to-noise ratio, enabling recovery of TOF-resolved dynamics without photon-limited bias.

Functional forearm measurement: vascular occlusion

Using the operating point established in phantom experiments, we performed *in vivo* measurements on the forearm of a healthy 43-year-old volunteer at a sweep rate of 50 kHz. To probe peripheral flow modulation, a standard blood-pressure cuff was used to transiently occlude arterial inflow. Measurements were acquired at three distinct stages: baseline (before cuff inflation), occlusion (cuff inflated to suprasystolic pressure), and release (immediately after cuff deflation). At the current stage of system development, continuous recordings over minutes-long protocols are not yet supported. Therefore, each condition was recorded consecutively in repeated short trials under identical optical settings.

Figure 4 summarizes the results for all three stages. The left column shows the retrieved temporal point-spread functions (TPSFs) with three representative time-of-flight (TOF) gates, while the center column shows the corresponding field autocorrelation functions $g_1(\tau_{s,}\tau_d)$. During baseline, later-arriving photons decorrelated more rapidly than early photons, consistent with longer photon path lengths and normal microvascular flow. Under occlusion, decorrelation slowed markedly across all TOF gates, with autocorrelation functions remaining elevated at long lags, reflecting the near absence of red blood cell motion. Following cuff release, the autocorrelation curves shifted toward faster decay, indicating a transient increase in blood flow consistent with reactive hyperaemia.

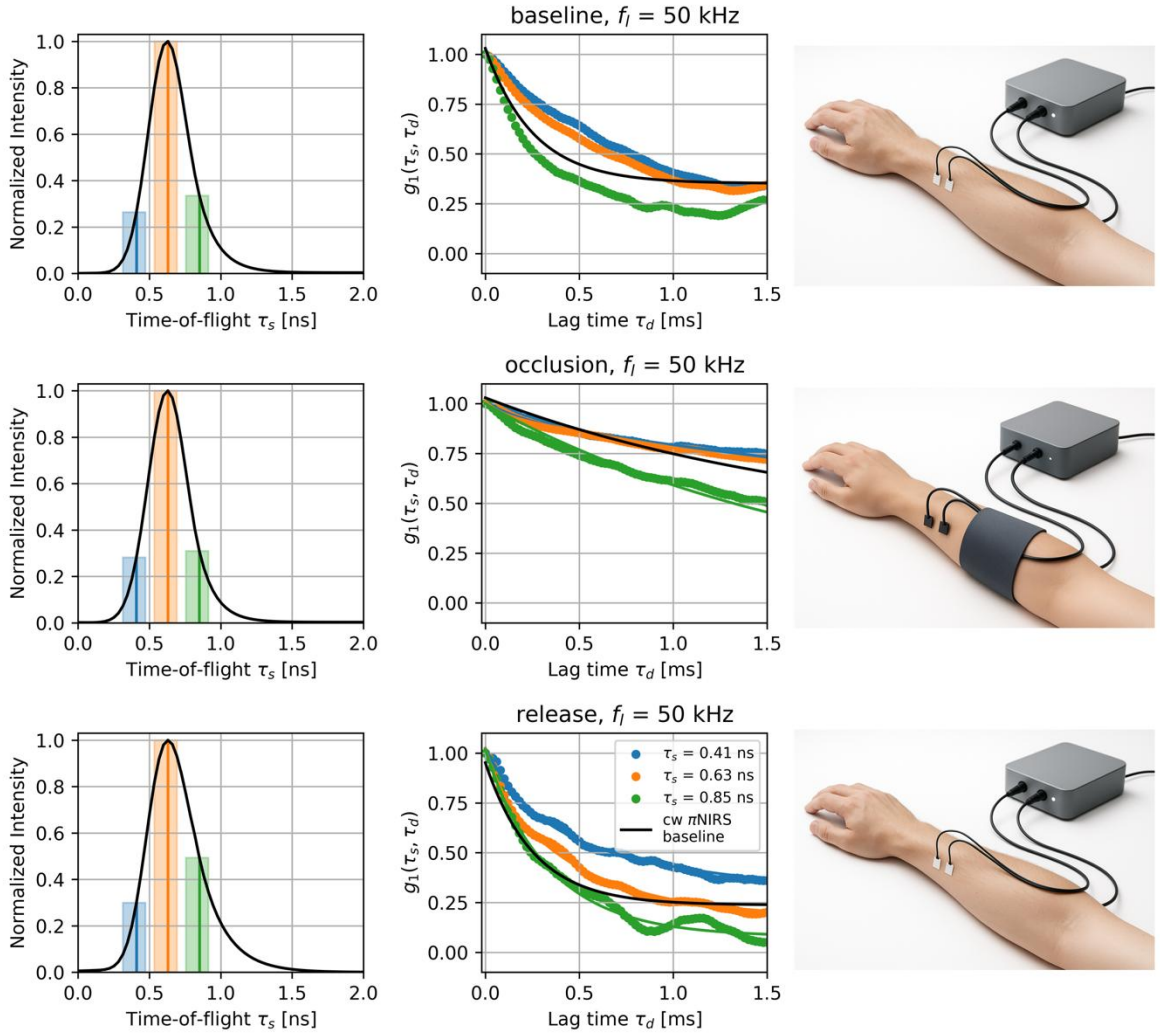

Fig. 4. Functional forearm measurement during vascular occlusion. Composite figure showing baseline, occlusion, and release conditions. Left: temporal point-spread functions (TPSFs) with three selected TOF gates. Center: corresponding field autocorrelation functions $g_1(\tau_{s,}\tau_d)$ for each gate. Right: rendering of the experimental setup. During occlusion, decorrelation slows markedly, while cuff release produces a transient overshoot consistent with reactive hyperaemia. All conditions were acquired in separate short trials at identical operating parameters.

Functional prefrontal measurement: superficial flow occlusion

To assess the sensitivity of the hybrid system to localized haemodynamic perturbations at the forehead, we performed a functional measurement using a tightened elastic headband. Increasing the pressure of the headband against the forehead partially occluded superficial scalp blood flow, while intracranial circulation was expected to remain largely unaffected due to the mechanical rigidity of the skull. Measurements were performed at a sweep rate of 50 kHz using the same operating parameters as in the forearm experiments.

Figure 5 summarizes the prefrontal measurements. The left column shows the temporal point-spread function (TPSF) together with the selected time-of-flight (TOF) gates, while the centre column presents the corresponding TOF-resolved field autocorrelation functions $g_1(\tau_s, \tau_d)$.

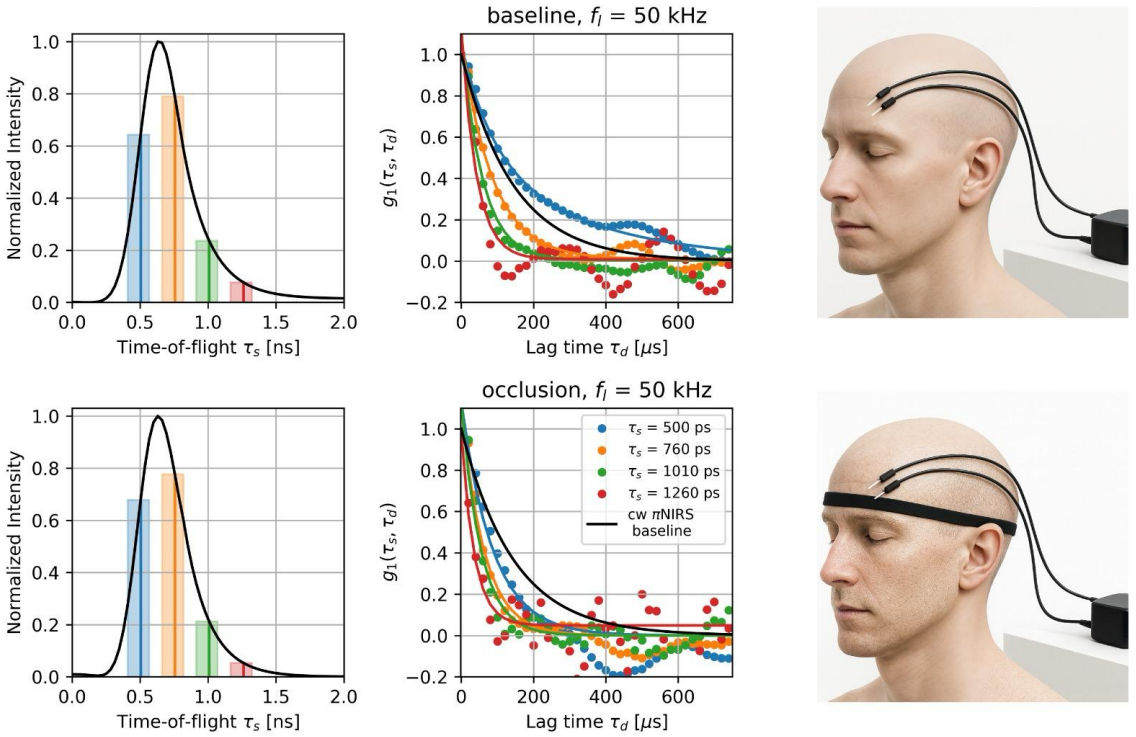

Fig. 5. Functional prefrontal measurement with superficial flow occlusion. Left: temporal point-spread functions (TPSFs) with selected TOF gates. Center: corresponding field autocorrelation functions $g_1(\tau_s,\tau_d)$ before and during headband tightening. Slower decorrelation is observed primarily for early TOF gates, reflecting reduced superficial scalp blood flow, while later TOF gates show weaker modulation due to preserved intracranial circulation. Right: rendering of the experimental setup using a tightened elastic headband.

Upon tightening the headband, the earliest analysed TOF gate (500 ps) exhibits a marked change in decorrelation behaviour. In particular, the effective decorrelation appears faster under compression, reflecting a reduction of slowly decorrelating superficial photon paths and a corresponding re-weighting toward deeper, more rapidly decorrelating contributions. Quantitative interpretation at this TOF is limited, however, as suppression of superficial dynamic scattering reduces signal-to-noise ratio, leading to large confidence intervals and reduced goodness of fit (Table 1). This gate therefore serves primarily as a qualitative indicator of superficial sensitivity rather than a robust quantitative measure.

At the intermediate TOF gate (760 ps), baseline and compression conditions yield comparable BFI values within overlapping confidence intervals, consistent with a transition regime in which photon paths sample a mixture of superficial and deeper tissue compartments. The magnitude of the compression-induced effect is reduced compared with the earliest gate, reflecting a gradual shift in depth sensitivity rather than abrupt compartmental separation.

In contrast, at later TOF gates (1010 ps and 1260 ps), effective BFI values are systematically higher under compression than at baseline, with good fit quality in both conditions. This behaviour should not be interpreted as increased blood flow during compression. Instead, it reflects a redistribution of the contributing photon-path ensemble following suppression of slowly decorrelating superficial components, such that the observed decorrelation becomes

increasingly dominated by deeper haemodynamic dynamics that remain largely preserved during headband tightening.

It is also noteworthy that baseline BFI values at latest TOF analyzed is modestly underestimated. Under baseline conditions, residual contributions from slowly decorrelating superficial paths persist at later lags, biasing mono-exponential fits toward smaller effective decay rates when long-lag points are included. This bias is reduced under compression, where superficial dynamics are attenuated, yielding more representative estimates of deeper-weighted decorrelation.

TOF, τ_s [ps]	Baseline			Occlusion		
	BFI	CI	R^2	BFI	CI	R^2
	[$\times 10^{-9}$ cm²/s]			[$\times 10^{-9}$ cm²/s]		
500	7.39	5.94–73.37	0.84	8.55	5.98–56.86	0.38
760	3.53	3.14–4.98	0.95	3.75	2.87–6.98	0.89
1 010	1.77	1.67–2.02	0.98	3.41	2.15–3.26	0.95
1 260	0.56	0.46–0.42	0.97	1.41	1.31–1.83	0.86

Table 1. Time-of-flight-resolved blood flow indices during superficial flow occlusion. Blood-flow indices (BFI) were obtained by fitting a mono-exponential decay model to the TOF-resolved field autocorrelation functions $g_1(\tau_s, \tau_d)$ at selected TOF gates during baseline and headband-compression conditions. Reported values correspond to TOF gates located in the trailing edge of the TPSF, where autocorrelation estimates remain physically meaningful under both conditions. Confidence intervals (CI) reflect reduced signal-to-noise ratio at early TOFs under compression due to suppression of superficial dynamic scattering. R^2 denotes the coefficient of determination of the fit.

For the analysis presented here, TOF-resolved autocorrelation functions were fitted using a mono-exponential decay model within a restricted lag window where the autocorrelation remained physically meaningful. While multi-component models can in principle separate superficial and deeper contributions, the mono-exponential approach adopted here provides a conservative and robust characterisation of TOF-dependent decorrelation dynamics, sufficient to demonstrate depth-dependent sensitivity in the presence of superficial perturbation.

It is also important to note that the absolute BFI values reported here likely represent conservative estimates. In the present analysis, the reduced scattering coefficient was fixed at $\mu_s' = 11.85\ \mathrm{cm}^{-1}$, which is higher than values commonly assumed in diffuse correlation and time-domain DCS studies of the adult head. Because the inferred blood-flow index scales inversely with μ_s', the use of a larger scattering coefficient naturally leads to smaller absolute BFIs. This choice does not affect the qualitative or relative trends reported here, which are the primary focus of this proof-of-principle experiment.

When interpreted in relative terms, the observed depth-dependent trends are consistent with prior time-domain diffuse correlation spectroscopy studies that explicitly exploited photon time-

of-flight gating to enhance depth sensitivity. Ozana *et al*. [39] demonstrated that superficial pressure modulation produces the largest relative reduction in blood-flow index at short source–detector separations and early time gates, while late time gates, which are more strongly weighted toward deeper tissue, exhibit substantially weaker modulation.

A comparable pattern is observed in the present measurements. Superficial compression leads to pronounced changes in early TOF gates, including reduced decorrelation contrast and degraded signal-to-noise ratio, while intermediate gates show attenuated responses and late TOF gates display relatively preserved decorrelation dynamics. Although the absolute BFI values differ due to differences in optical parameters, instrumentation, and analysis models, the relative depth-dependent response and strong superficial sensitivity with diminishing modulation at later time gates, which closely matches the behaviour reported for functional time-domain DCS. This agreement supports the interpretation that TOF gating provides a robust mechanism for separating superficial and deeper haemodynamic contributions, even in the absence of large source–detector separations.

Overall, this experiment demonstrates that the hybrid system can distinguish between superficial and deeper haemodynamic changes using TOF-resolved autocorrelation analysis, even when the perturbation is confined to extracerebral tissue. The depth-dependent divergence in decorrelation behaviour—strong effects at early TOFs and relative preservation at late TOFs—highlights the value of TOF-resolved measurements and underscores the limitations of TOF-integrated approaches for separating superficial and deeper vascular contributions.

Discussion

This work demonstrates a hybrid iNIRS platform that combines the time-of-flight (TOF) sensitivity of interferometric NIRS with the photon efficiency of parallel detection. By merging swept-source interferometry with camera-based readout, we establish an operating regime in which both photon starvation and electronic-bandwidth ceilings are mitigated. Our experiments, spanning controlled ceiling demonstrations, liquid phantoms, and progressively more complex proof-of-principle *in vivo* measurements (N = 1) on the forearm and forehead, show that this approach enables recovery of blood-flow dynamics that are inaccessible to either single-channel iNIRS or CW-πNIRS alone.

The motivation for the hybrid design lies in the complementarity of existing modalities. iNIRS provides excellent TOF resolution but is photon-starved due to single-mode fibre collection. CW-πNIRS and related parallel-speckle approaches achieve high photon throughput through spatial multiplexing but lack TOF sectioning and are constrained by MHz-class camera electronics. By integrating these architectures, hybrid iNIRS achieves nanosecond-scale TOF resolution together with multi-speckle averaging, enabling improved signal-to-noise ratio (SNR) and faster temporal sampling. Importantly, the platform is not a simple merger of techniques: identifying viable operating windows required careful calibration of sweep rate, sampling density, photon budget, and camera throughput. Each experimental stage therefore served both to validate system performance and to map the parameter space relevant for future implementations.

Developing a stable platform required addressing several technical challenges. Stable swept-source operation, reliable k-linearisation, and consistent performance under physiological flows demanded iterative optimisation. The underlying design trade-offs are fundamental. By increasing sweep rate, we improve temporal sampling but reduce photons per sweep. On the other hand, increasing tuning bandwidth sharpens TOF resolution but shortens the usable TOF window and detector sampling rate ultimately limits the accessible dynamic range. Our results illustrate how balancing these factors determines whether depth-resolved flow can be recovered in practice.

Relative to other approaches, hybrid iNIRS aligns with the goals of multi-speckle detection methods such as SPAD arrays, speckle contrast optical spectroscopy, and interferometric diffusing-wave spectroscopy, all of which aim to improve SNR through parallelisation. Conceptually, the system can also be viewed in the context of swept-source OCT. Whereas OCT prioritises micron-scale axial resolution using very broad bandwidths, hybrid iNIRS employs sweeps that are approximately three orders of magnitude narrower to favour nanosecond-scale depth gating in highly scattering tissue. In this sense, the present architecture adapts OCT-inspired interferometric reference designs to the photon-limited regime of diffuse optics.

Several limitations remain. The current prototype operates at a single wavelength and moderate sweep rates, limiting chromophore specificity and dynamic range. The in vivo results presented here are intended as proof-of-concept demonstrations in a single volunteer (N = 1) and do not yet address inter-subject variability, motion robustness, or long-duration monitoring. Moreover, the balance between sweep speed, depth sectioning, and photon budget remains delicate, and further optimisation will be required for translation to routine neuroimaging.

The functional measurements presented here nevertheless illustrate the potential of hybrid iNIRS. Forearm cuff occlusion reproduced the expected suppression of flow during blockage and a hyperaemic overshoot upon release, while forehead measurements using a tightened elastic headband demonstrated selective modulation of superficial scalp circulation. Importantly, late-arriving photon gates probing deeper tissue showed weaker modulation during forehead compression, consistent with preserved intracranial flow. Although demonstrated in a single subject, these experiments highlight the value of TOF-resolved measurements for distinguishing superficial from deeper haemodynamic contributions and motivate future studies in larger cohorts.

It is important to note that the present implementation does not yet constitute a fully parallel iNIRS system. The prototype combines a single-mode iNIRS arm with a parallel camera arm, enabling simultaneous TOF sectioning and multi-speckle averaging, but at limited sweep rates. A true parallel iNIRS platform, in which all speckles are captured at full TOF resolution, will likely require computational approaches to effectively upsample sweeps beyond the raw camera frame rate. Advances in laser stability, data-acquisition electronics, and algorithmic reconstruction will be necessary to realise such a system. In this sense, the hybrid approach represents a pragmatic and scalable intermediate step that demonstrates feasibility while outlining a clear pathway toward fully parallel TOF-resolved interferometric monitoring.

Future work will focus on extending the system to multi-wavelength operation for spectroscopic separation of haemoglobin species, integrating computational methods to increase effective sweep rates without exceeding camera bandwidth, and scaling to higher channel counts to further improve photon budgets. These developments will build on the present foundation and move hybrid iNIRS toward a robust platform for non-invasive brain monitoring.

Conclusions

We introduced a hybrid iNIRS platform that unites the time-of-flight sensitivity of interferometric NIRS with the photon efficiency of parallel detection. Through ceiling analyses, liquid phantom studies, and proof-of-principle in vivo measurements in a single volunteer (N = 1) on the forearm and forehead, we demonstrated TOF-resolved recovery of blood-flow dynamics that are inaccessible to conventional single-channel or continuous-wave approaches. Conceptually, the platform extends multi-speckle strategies while bridging toward swept-source full-field OCT. Looking ahead, scalability through multi-wavelength operation, computational upsampling to approach full parallel iNIRS, and higher channel counts with advances in compact swept sources and high-speed cameras could potentially enable portable and wearable systems. Such devices would complement established modalities such as EEG and fMRI, opening a path toward continuous, non-invasive monitoring of cerebral and peripheral haemodynamics.

Methods

In this section, we describe the experimental and analytical framework used to implement and validate the hybrid iNIRS system. We first present the optical architecture, including the shared swept-source laser and the three coordinated detection paths that form the hybrid configuration. We next outline the signal acquisition and processing pipeline for time-of-flight (TOF) reconstruction and field-autocorrelation analysis. Finally, we detail the experimental procedures used to evaluate system performance, starting with controlled liquid phantoms with tunable optical properties and progressing to *in vivo* measurements on human subjects to assess feasibility for cerebral blood-flow monitoring.

Optical system

The optical layout of the hybrid iNIRS system is presented in Figure 6. The setup comprises a tuneable laser source, three interferometers, a digitizer, and a PC for data acquisition and signal processing. The light source was a tuneable laser diode centred at λ_c = 780 nm (EYP-DFB-0780-

00020-1500-BFY12-0005, Eagleyard-Toptica) with $\delta\lambda_{FWHM}$ of 0.6 MHz (1.2 fm). The laser output was divided into two paths: a sample beam (70%) and a reference beam (30%) using an optical fibre splitter. The sample beam illuminated the target (e.g. biological tissue) and was collected by optical fibres (navy blue and yellow in Fig. 6). The reference beam was further split into three channels using an additional optical splitter, each directed to one of the system sub-units. The output signals from these sub-units were digitised using an acquisition card (M2p.5962-x4, Spectrum Instrumentation) connected to the PC, where they were processed numerically.

The reference interferometer (Fig. 6, bottom right) was implemented as a fibre-based Mach–Zehnder interferometer with a fixed optical path-length difference of 2 m. Its output was coupled via a 2x2 50:50 fibre coupler to a balanced photodetector (PDB450A-AC, Thorlabs), which converted the optical interference signal into an electrical voltage. This was used to convert the optical interference signal into an electrical voltage signal.

The iNIRS detection sub-unit (Fig. 6, bottom centre) was realised as a Mach–Zehnder interferometer in which the reference beam (propagating in a single-mode fibre, SMF, marked in orange in Fig. 8) and the measurement beam (SMF, yellow) were combined in a 2x2 50:50 optical coupler whose outputs were connected to a balanced detector (PDB450A-AC, Thorlabs)

The parallel interferometric NIRS (πNIRS) sub-unit (Figure 6, bottom left) was implemented as a free-space Mach–Zehnder interferometer. Here, the reference beam (SMF, orange) and the measurement beam (multi-mode fibre, navy blue) were collimated, directed onto a 90R:10T beam splitter, and the resulting interference pattern was recorded using a 2D CMOS sensor (Fastcam Nova S16, Photron) operating at a frame rate of 1.1 MHz.

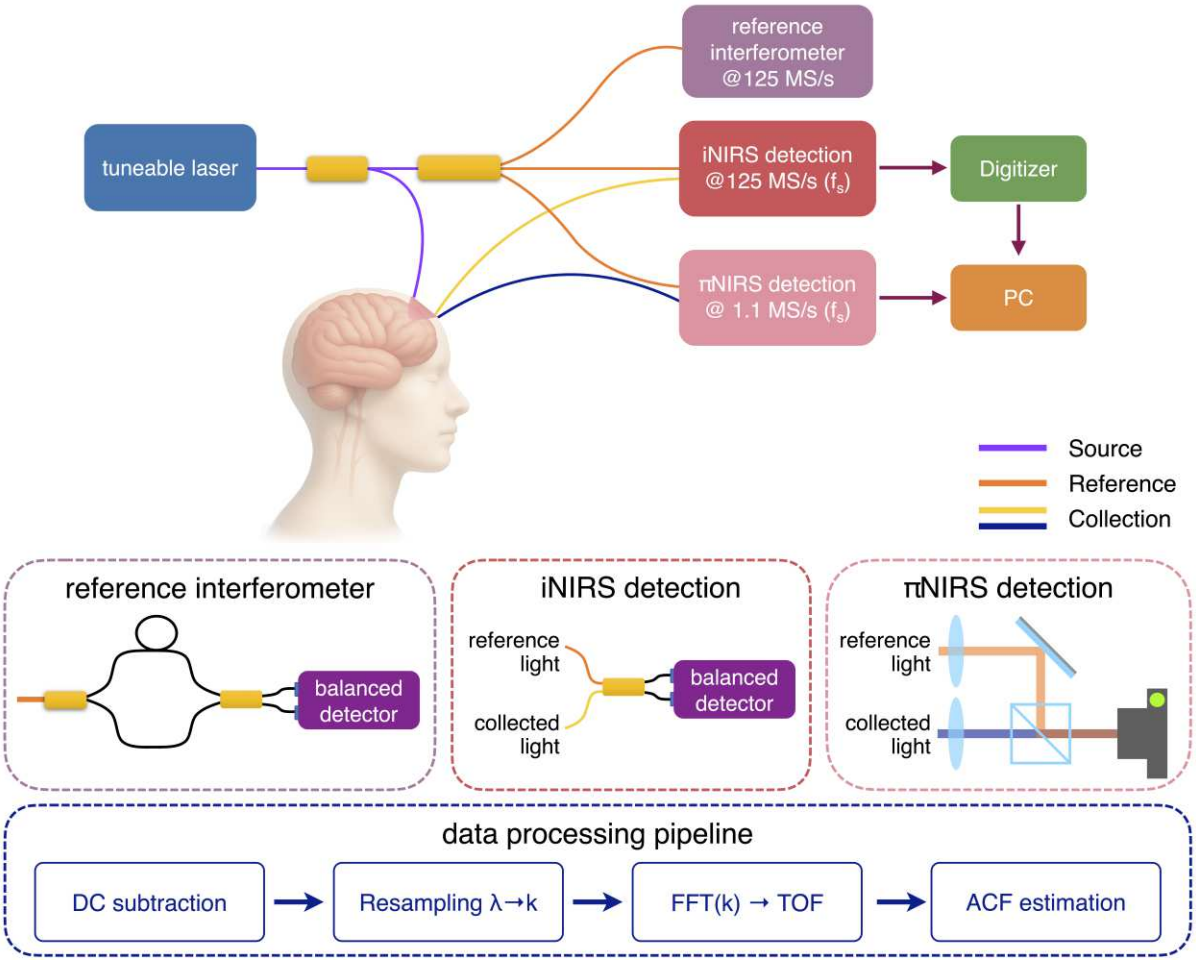

Fig. 6. Hybrid interferometric NIRS architecture. A single swept-source laser is distributed across three coordinated detection paths: (i) a reference interferometer providing wavenumber calibration and source fluctuation monitoring, (ii) a single-mode iNIRS detection arm digitized at 125 MS/s for precise TOF fidelity and phase stability, and (iii) a πNIRS detection arm imaging multiple speckle modes onto a 1.1 MHz CMOS sensor for high photon throughput. Data streams are synchronized by a common digitizer and processed on a PC. This architecture combines the timing precision of classical iNIRS with the throughput of πNIRS, while maintaining calibration stability via the reference interferometer.

Acquisition protocol

The hybrid iNIRS system can operate in two distinct modes: time-of-flight (TOF) and continuous-wave (CW). In the TOF mode, the waveform generator provided both an electrical trigger signal to initiate acquisition and a sawtooth voltage waveform that modulated the laser diode current via the controller (CTL200-1-B-200, Koheron). The modulation caused the laser wavelength to sweep proportionally to the peak-to-peak amplitude (V_{pp}). During TOF operation, signals from the reference interferometer and the iNIRS sub-units were recorded. For low sweep frequencies, signals from the πNIRS sub-unit were also acquired and analysed.

In the CW mode, the measurement was triggered only once at the beginning of acquisition, with no wavelength modulation applied. The laser diode therefore remained fixed at its central wavelength throughout the recording. In this mode, only signals from the πNIRS sub-unit were

recorded and analysed. TOF and CW measurements were performed sequentially under identical optical conditions.

The tuneable laser was driven by a sawtooth waveform generated by a function generator. This drive served two purposes: (i) to actuate the wavelength sweep, and (ii) to provide a stable cycle reference used to segment the continuous data streams into individual sweeps for subsequent numerical processing.

Signal processing

All three detection paths were acquired and processed within a unified computational pipeline (Fig. 7). The iNIRS and the reference interferometer channels were sampled at 125 MS/s, and the πNIRS frames were recorded at a line rate of 1.1 MHz.

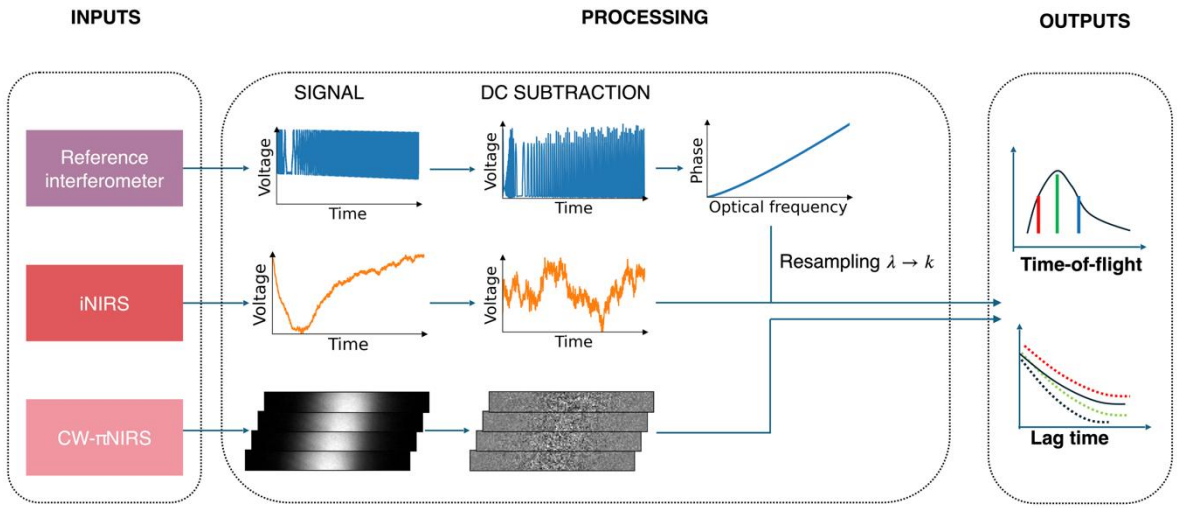

Fig. 7. *Signal processing pipeline for hybrid interferometric NIRS.* Inputs from the three detection arms (reference interferometer, single-mode iNIRS, and parallel πNIRS) are segmented using the sawtooth sweep reference, followed by DC subtraction and detrending. For iNIRS, resampling from wavelength to wavenumber enables Fourier transformation to obtain TOF-resolved complex signals. Within selected TOF gates, complex field samples across sweeps yield TOF-resolved autocorrelations, $g_1(\tau_s, \tau_d)$. In CW-πNIRS mode, the laser operates without tuning, producing TOF-integrated autocorrelations $g_1(\tau_d)$. The outputs are TOF distributions (photon arrival statistics) and lag-dependent autocorrelations that describe decorrelation dynamics.

Raw signal segmentation and preprocessing

Raw traces from all channels (trigger, iNIRS, and reference) were segmented sweep by sweep using the sawtooth modulation reference and trigger events. Each sweep was DC-subtracted and detrended using a short moving window to suppress baseline drifts and residual slopes.

iNIRS processing

A resampling vector was generated from the reference interferometer signal. Each sweep was resampled from wavelength to wavenumber ($\lambda \rightarrow k$) on a uniform grid to ensure phase-linear sampling and enable accurate TOF reconstruction. The resampled and detrended sweeps were zero-padded and Fourier-transformed to obtain the complex-valued functions Γ_{rs}. The temporal

average of their squared magnitude yielded the temporal point-spread function (TPSF). A background record (sample arm blocked) was acquired under identical conditions, processed identically, and subtracted before further analysis.

Within the selected TOF gate (near the TPSF peak), complex field samples across consecutive sweeps were correlated to compute the field autocorrelation $g_1(\tau_s, \tau_d)$ at discrete lags determined by the sweep rate.

πNIRS processing

For the πNIRS data, intensity time series were extracted for every camera pixel (each corresponding to an independent speckle). These traces were resampled, zero-padded, and Fourier-transformed to generate per-pixel TPSFs and autocorrelations, which were then ensemble-averaged across all pixels.

CW-πNIRS reference mode

In the CW-πNIRS mode, the laser operated without wavelength tuning. Speckle intensity fluctuations were recorded at 1.1 MHz across all camera pixels. After DC subtraction, pixel time courses were used to estimate the field autocorrelation $g_1(\tau_d)$, which was subsequently ensemble-averaged. In principle, the CW-πNIRS $g_1(\tau_d)$ corresponds to the TOF-integrated iNIRS autocorrelation. Deviations between the two indicate instrumental instabilities or parameter misalignment in the iNIRS processing chain.

Autocorrelation correction and outputs

In all cases, the first-lag bias of the autocorrelation functions was corrected using the background estimate, and residual offsets were removed by averaging the long-lag tail and subtracting it from all lags.

The complete pipeline therefore produced two key outputs:

- TOF distributions $I_s(\tau_s)$ describing depth-resolved photon arrival statistics,
- Lag-dependent autocorrelations $g_1(\tau_s, \tau_d)$ quantifying temporal decorrelation dynamics and blood-flow sensitivity

Tissue-mimicking liquid phantoms

Liquid tissue phantoms were prepared by mixing commercial whole milk (3.2 % fat content) and distilled water in a 1:1 volume ratio to achieve optical properties comparable to biological tissue. The mixture was thoroughly stirred to ensure uniform scattering and then poured into a glass beaker. The beaker was sealed with a 3D-printed lid containing dedicated openings for the illumination fibre (centrally positioned) and the collection fibres, which were arranged symmetrically around the illumination point at a source–detector separation of 10 mm.

In vivo measurements

In vivo measurements were performed on a healthy 43-year-old male volunteer. The optical power at the fibre output was maintained at 15 mW, and the total exposure time for a single measurement did not exceed 5 s. All experimental procedures and protocols were reviewed and approved by the Commission of Bioethics at the Military Institute of Medicine, Poland (permission no. 90/WIM/2018). The experiments were conducted following the tenets of the Declaration of

Helsinki. Written informed consent was obtained from all subjects before measurements, and all possible risks related to the examination were explained. The source–detector fibre separation was 10 mm, with the fibres mounted in a 3D-printed elastic holder and secured to the forehead or forearm using an adjustable band.

Safety limits were evaluated according to the ANSI Z136.1-2014 standard. For skin exposure in the near-infrared spectral range (700–1050 nm), the maximum permissible exposure (MPE) is defined as $0.2 \cdot C_A$ W·cm^{-2} (ANSI Z136.1-2014, Table 7b), where the wavelength-dependent correction factor is $C_A = 10^{0.002(\lambda-700)}$ (ANSI Z136.1-2014, Table 6a). Assuming an illumination wavelength of 780 nm, the corresponding MPE level is 289.1 mW·cm^{-2}. For optical-fibre delivery, the limiting aperture used in MPE calculations is 3.5 mm in diameter (ANSI Z136.1-2014, Table 8a), corresponding to an effective area of 9.62×10^{-2} cm^2 (ANSI Z136.1-2014, Table 8b). Under these assumptions, the maximum irradiance of our system was 155.9 mW·cm^{-2}, which remains safely below the ANSI limits for skin exposure.

Optical and dynamical property fitting

Optical-property fitting was performed by modelling photon propagation in tissue using the semi-infinite solution to the diffusion equation. To account for the temporal characteristics of the system, the theoretical model was convolved with the experimentally measured instrument response function (IRF) prior to comparison with the data. The resulting forward model was fitted to the experimental time-resolved measurements, enabling extraction of the absorption coefficient (μ_a) and the reduced scattering coefficient (μ_s'), which characterise the bulk optical properties of the medium.

For dynamical property estimation, the temporal field autocorrelation function was analysed using exponential decorrelation models. In the most general case, a bi-exponential model was employed,

$$g_1(\tau_s, \tau_d) = a(\tau_s) \exp[-b(\tau_s)\tau_d] + c(\tau_s), \tag{6}$$

where $a(\tau_s)$ is the amplitude, $b(\tau_s)$ is the corresponding TOF-dependent decay rate, and $c(\tau_s)$ is a long-delay offset accounting for noise and residual correlations.

From the extracted decorrelation rate $b(\tau_s)$ (or $d(\tau_s)$), when the slow component dominated) and the reduced scattering coefficient μ_s', the blood-flow index (BFI, αD_B) was estimated following standard diffusing-wave spectroscopy theory [40, 41]:

$$\alpha D_B(\tau_s) = \frac{b(\tau_s) n}{2k^2 \mu_s' c \tau_s}, \tag{7}$$

where n is the refractive index of the medium, $k = 2\pi n/\lambda_c$ is the in-medium wavenumber, λ_c is the centre wavelength, and c is the speed of light in vacuum. This relation links the TOF-dependent decorrelation rate to an effective Brownian diffusion coefficient scaled by flow, thereby connecting the measured autocorrelation dynamics with underlying haemodynamic processes in tissue.

System optimisation

In our configuration, the illumination and detection points are separated by a finite distance, placing the measurement firmly in the diffusion regime. Under these conditions, injected light undergoes extensive multiple scattering and is strongly attenuated before reaching the detector. Diffusion theory predicts that only ~10^{-6} of the launched photons are collected. Interferometric detection is therefore essential, as coherent mixing with a stronger reference arm provides optical amplification of the weak diffuse field. This amplification must, however, be carefully controlled. If the reference power is too high, it suppresses the relative fluctuations of the sample field and reduces the visibility of dynamic components.

To optimise the signal-to-noise ratio (SNR), the reference power in the iNIRS arm must remain within an appropriate operating range. Excessive reference power causes the sample contribution to be dominated by laser technical noise, including residual intensity fluctuations. Conversely, insufficient reference power reduces heterodyne efficiency and degrades SNR. Illumination power at the sample must also be sufficient to ensure that, after strong attenuation in tissue, the returning diffuse field remains detectable. These dependencies are illustrated in Fig. 8.

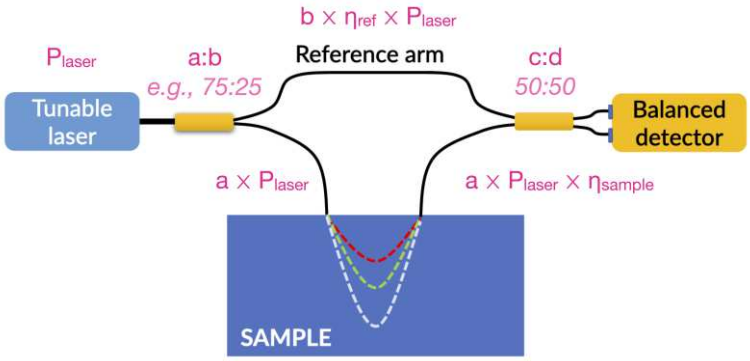

Fig. 8. *Power levels analysis for iNIRS system.* P_l, a:b, c:d, η_s and η_r denote the laser output power, splitter ratios, coupler ratio, and sample/reference attenuation factors, respectively.

A balanced detector consists of two matched photodiodes whose photocurrents are electronically subtracted and amplified. This configuration strongly suppresses common-mode noise, including intensity fluctuations originating from the laser, and removes the large DC terms that do not carry interferometric information. In a fibre-based implementation, the final 50:50 coupler before the detector introduces a relative π-phase shift between its two output ports. As a result, the optical fields reaching the two photodiodes differ by this π phase, ensuring that the interference terms appear with opposite signs. When the two photocurrents are subtracted, the DC components cancel while the heterodyne terms add constructively, yielding an improved signal-to-noise ratio.

The intensities at the two inputs of the balanced detector can therefore be written as:

$$I_{BD,1} = c\left[(b \cdot \eta_r \cdot P_l)^2 + (a \cdot \eta_s \cdot P_l)^2 + 2 \cdot P_l \cdot \sqrt{ab \cdot \eta_s \cdot \eta_r}\cos(\Delta\phi)\right], \quad (8)$$

$$I_{BD,2} = d\left[(b \cdot \eta_r \cdot P_l)^2 + (a \cdot \eta_s \cdot P_l)^2 + 2 \cdot P_l \cdot \sqrt{ab \cdot \eta_s \cdot \eta_r}\cos(\Delta\phi)\right], \quad (9)$$

where $I_{BD,1}$ and $I_{BD,2}$ are the signal intensities at the balance detector inputs, Pl is the laser's output power level, a:b is the first splitter ratio, c:d is the coupling ratio of the coupler connected with the balanced detector's inputs, Δϕ is the phase difference between the sample field and the reference field, η_s and η_r are attenuation factors in the sample, and reference paths, respectively.

The combined output of the balanced detector is obtained by subtracting the photocurrents generated by the two photodiodes. Because the final 50:50 fibre coupler introduces a relative π-phase shift between its output ports, the interference terms at the two detector inputs appear with opposite signs, whereas the DC terms remain identical. Subtraction therefore removes the large DC background, arising from the individual powers in the sample and reference arms, and suppresses laser intensity noise that is common to both photodiodes. At the same time, the heterodyne term is preserved and effectively doubled, providing improved interferometric sensitivity.

The balanced-detector output can be expressed as:

$$I_{BD} = I_{BD,1} - I_{BD,2}e^{i\pi}, \tag{10}$$

where the factor $e^{i\pi} = -1$ is the π-phase shift induced by the fibre coupler. For a 50:50 coupling ratio (c=d=0.50), the subtraction removes all DC components and simplifies the output to:

$$I_{BD} = 2P_l\sqrt{ab \cdot \eta_r \cdot \eta_s}\cos(\Delta\phi). \tag{11}$$

Equation (11) shows that the detected heterodyne signal scales with the geometric mean of the sample and reference powers, modulated by the phase difference $\Delta\phi$. This theoretical relationship allows optimisation of the optical splitting ratios. A 50:50 fibre coupler (c:d = 1:1) maximises balanced-detector performance by ensuring complete DC cancellation and doubling of the interference term. For the first splitter, a ratio of a:b = 75:25 provides an optimal compromise between sample-arm illumination and reference-arm power, ensuring that the reference field is strong enough to maximise heterodyne gain while keeping laser technical noise below the sample-induced fluctuations.

In addition to the theoretical analysis, we experimentally evaluated several practical splitter configurations to validate Eq. (11). For the first splitter, ratios of 99:1, 90:10 and 75:25 were tested, while for the second (final) coupler, ratios of 50:50, 90:10 and 99:1 were investigated. In all cases, the measured interferometric signal amplitudes showed clear agreement with the dependence predicted by Eq. (11), confirming that the detected heterodyne term scales with the geometric mean of the sample and reference powers. The results consistently indicated that a 50:50 fibre coupler maximises balanced-detector performance by ensuring complete DC cancellation and doubling of the interference term, whereas a 75:25 ratio for the first splitter provides the best compromise between sufficient reference power and optimal sample illumination.

Funding Declaration

This work was supported by the National Science Centre (Poland) under grant no. 2022/46/E/ST7/00291.

References

1. Durduran, T. and A.G. Yodh, *Diffuse correlation spectroscopy for non-invasive, micro-vascular cerebral blood flow measurement.* Neuroimage, 2014. **85 Pt 1**(0 1): p. 51-63.
2. Thomas, R., S.S. Shin, and R. Balu, *Applications of near-infrared spectroscopy in neurocritical care.* Neurophotonics, 2023. **10**(2): p. 023522.
3. Mathieu, F., et al., *Continuous Near-infrared Spectroscopy Monitoring in Adult Traumatic Brain Injury: A Systematic Review.* J Neurosurg Anesthesiol, 2020. **32**(4): p. 288-299.
4. Yang, M., et al., *A Systemic Review of Functional Near-Infrared Spectroscopy for Stroke: Current Application and Future Directions.* Front Neurol, 2019. **10**: p. 58.
5. Reynolds, E.O., et al., *New non-invasive methods for assessing brain oxygenation and haemodynamics.* Br Med Bull, 1988. **44**(4): p. 1052-75.
6. Boas, D.A., et al., *Twenty years of functional near-infrared spectroscopy: introduction for the special issue.* Neuroimage, 2014. **85 Pt 1**: p. 1-5.
7. Jobsis, F.F., *Noninvasive, infrared monitoring of cerebral and myocardial oxygen sufficiency and circulatory parameters.* Science, 1977. **198**(4323): p. 1264-7.
8. Jacques, S.L., *Optical properties of biological tissues: a review.* Phys Med Biol, 2013. **58**(11): p. R37-61.
9. Strangman, G.E., Z. Li, and Q. Zhang, *Depth sensitivity and source-detector separations for near infrared spectroscopy based on the Colin27 brain template.* PLoS One, 2013. **8**(8): p. e66319.
10. Scholkmann, F., et al., *A review on continuous wave functional near-infrared spectroscopy and imaging instrumentation and methodology.* Neuroimage, 2014. **85 Pt 1**: p. 6-27.
11. Ferrari, M. and V. Quaresima, *A brief review on the history of human functional near-infrared spectroscopy (fNIRS) development and fields of application.* Neuroimage, 2012. **63**(2): p. 921-35.
12. Tachtsidis, I. and F. Scholkmann, *False positives and false negatives in functional near-infrared spectroscopy: issues, challenges, and the way forward.* Neurophotonics, 2016. **3**(3): p. 031405.
13. Gagnon, L., et al., *Short separation channel location impacts the performance of short channel regression in NIRS.* Neuroimage, 2012. **59**(3): p. 2518-28.
14. Caldwell, M., et al., *Modelling confounding effects from extracerebral contamination and systemic factors on functional near-infrared spectroscopy.* Neuroimage, 2016. **143**: p. 91-105.
15. Fantini, S. and A. Sassaroli, *Frequency-Domain Techniques for Cerebral and Functional Near-Infrared Spectroscopy.* Front Neurosci, 2020. **14**: p. 300.
16. Torricelli, A., et al., *Time domain functional NIRS imaging for human brain mapping.* Neuroimage, 2014. **85 Pt 1**: p. 28-50.
17. Pifferi, A., et al., *New frontiers in time-domain diffuse optics, a review.* J Biomed Opt, 2016. **21**(9): p. 091310.
18. Liebert, A., et al., *Evaluation of optical properties of highly scattering media by moments of distributions of times of flight of photons.* Appl Opt, 2003. **42**(28): p. 5785-92.
19. Liebert, A., et al., *Time-resolved multidistance near-infrared spectroscopy of the adult head: intracerebral and extracerebral absorption changes from moments of distribution of times of flight of photons.* Appl Opt, 2004. **43**(15): p. 3037-47.
20. Carp, S.A., M.B. Robinson, and M.A. Franceschini, *Diffuse correlation spectroscopy: current status and future outlook.* Neurophotonics, 2023. **10**(1): p. 013509.
21. James, E. and P.R.T. Munro, *Diffuse Correlation Spectroscopy: A Review of Recent Advances in Parallelisation and Depth Discrimination Techniques.* Sensors (Basel), 2023. **23**(23).
22. Borycki, D., et al., *Interferometric Near-Infrared Spectroscopy (iNIRS) for determination of optical and dynamical properties of turbid media.* Optics Express, 2016. **24**(1): p. 329-354.
23. Borycki, D., O. Kholiqov, and V.J. Srinivasan, *Interferometric near-infrared spectroscopy directly quantifies optical field dynamics in turbid media.* Optica, 2016. **3**(12): p. 1471-1476.
24. Borycki, D., O. Kholiqov, and V.J. Srinivasan, *Correlation gating quantifies the optical properties of dynamic media in transmission.* Opt Lett, 2018. **43**(23): p. 5881-5884.
25. Borycki, D., O. Kholiqov, and V.J. Srinivasan, *Reflectance-mode interferometric near-infrared spectroscopy quantifies brain absorption, scattering, and blood flow index in vivo.* Opt Lett, 2017. **42**(3): p. 591-594.

26. Mazumder, D., O. Kholiqov, and V.J. Srinivasan, *Interferometric near-infrared spectroscopy (iNIRS) reveals that blood flow index depends on wavelength*. Biomedical Optics Express, 2024. **15**(4): p. 2152-2174.
27. Kholiqov, O., et al., *Time-of-flight resolved light field fluctuations reveal deep human tissue physiology*. Nat Commun, 2020. **11**(1): p. 391.
28. Samaei, S., et al., *Time-domain diffuse correlation spectroscopy (TD-DCS) for noninvasive, depth-dependent blood flow quantification in human tissue in vivo*. Sci Rep, 2021. **11**(1): p. 1817.
29. Sutin, J., et al., *Time-domain diffuse correlation spectroscopy*. Optica, 2016. **3**(9): p. 1006-1013.
30. Poon, C.S., et al., *First-in-clinical application of a time-gated diffuse correlation spectroscopy system at 1064 nm using superconducting nanowire single photon detectors in a neuro intensive care unit*. Biomed Opt Express, 2022. **13**(3): p. 1344-1356.
31. Mogharari, N., et al., *Time-domain diffuse correlation spectroscopy at large source detector separation for cerebral blood flow recovery*. Biomedical Optics Express, 2024. **15**(7): p. 4330-4344.
32. Dietsche, G., et al., *Fiber-based multispeckle detection for time-resolved diffusing-wave spectroscopy: characterization and application to blood flow detection in deep tissue*. Applied Optics, 2007. **46**(35): p. 8506-8514.
33. Wayne, M.A., et al., *Massively parallel, real-time multispeckle diffuse correlation spectroscopy using a 500 x 500 SPAD camera*. Biomed Opt Express, 2023. **14**(2): p. 703-713.
34. Kim, B., et al., *Mapping human cerebral blood flow with high-density, multi-channel speckle contrast optical spectroscopy*. bioRxiv, 2025: p. 2025.03.03.638332.
35. Zhou, W., et al., *Functional interferometric diffusing wave spectroscopy of the human brain*. Sci Adv, 2021. **7**(20).
36. Samaei, S., et al., *Continuous-wave parallel interferometric near-infrared spectroscopy (CW piNIRS) with a fast two-dimensional camera*. Biomed Opt Express, 2022. **13**(11): p. 5753-5774.
37. Mandracchia, B., et al., *High-speed optical imaging with sCMOS pixel reassignment*. Nat Commun, 2024. **15**(1): p. 4598.
38. Borycki, D., et al., *Multiwavelength laser doppler holography (MLDH) in spatiotemporal optical coherence tomography (STOC-T)*. Biocybernetics and Biomedical Engineering, 2024. **44**(1): p. 264-275.
39. Ozana, N., et al., *Functional Time Domain Diffuse Correlation Spectroscopy*. Front Neurosci, 2022. **16**: p. 932119.
40. Pine, D.J., et al., *Diffusing wave spectroscopy*. Phys Rev Lett, 1988. **60**(12): p. 1134-1137.
41. Yodh, A.G., P.D. Kaplan, and D.J. Pine, *Pulsed diffusing-wave spectroscopy: High resolution through nonlinear optical gating*. Phys Rev B Condens Matter, 1990. **42**(7): p. 4744-4747.

Supplementary Files

This is a list of supplementary files associated with this preprint. Click to download.

- SupplementaryInformation.docx